processes

MDPI

Article

Numerical Simulation of Multiphase Dust Transport Law and Scaled Model Testing of Spray Suppression Mechanism in Tunnel Blasting

Fayi Deng [1], Kaifu Ren [1], Guofeng Wang [1], Yongqiao Fang [1], Jiayu Zhou [2] and Heng Zhang [2,*]

[1] Guizhou Road and Bridge Group Co., Ltd., Guiyang 550001, China; fayideng@126.com (F.D.); renkaifu398271@163.com (K.R.); wangguofeng741321@163.com (G.W.); fangyongqiao365214@163.com (Y.F.)
[2] Key Laboratory of Transportation Tunnel Engineering, Ministry of Education, Southwest Jiaotong University, Chengdu 610031, China; w5516831@163.com
* Correspondence: tunnelzh@swjtu.edu.cn; Tel.: +86-028-87634386

Abstract

Tunnel construction in western China is developing towards deeper burial, larger cross-sections, and longer distances. Dust and other pollutants generated during drill-and-blast construction endanger construction safety and workers' health, making research on their migration and dust removal measures of great significance. This paper, based on the Zimuyan Tunnel, studies the dust migration characteristics and water mist dust removal schemes through three-dimensional numerical simulation (ICEM CFD modeling, Fluent analysis), 1:20 model tests, and on-site monitoring. The results show that eddies form at the working face in the later stage of ventilation, and dust exhibits vertical stratification due to differences in particle size; the nozzle angle and flow rate significantly affect the dust removal efficiency, and reasonable adjustment can improve the efficiency while reducing the impact on airflow; notably, both nozzle angle and flow rate affect in-tunnel airflow. The conclusion is that the distance of the air duct outlet should be adjusted to reduce the pressure difference to avoid eddies, and the nozzle angle and flow rate should be moderately adjusted to optimize the dust removal effect.

Keywords: extra-long tunnel; drill-and-blast construction; construction ventilation; pollutant transport law; water mist dust removal; numerical calculation; model test

check for updates

Academic Editor: Haiping Zhu

Received: 17 August 2025
Revised: 9 September 2025
Accepted: 11 September 2025
Published: 17 September 2025

Citation: Deng, F.; Ren, K.; Wang, G.; Fang, Y.; Zhou, J.; Zhang, H. Numerical Simulation of Multiphase Dust Transport Law and Scaled Model Testing of Spray Suppression Mechanism in Tunnel Blasting. *Processes* **2025**, *13*, 2959. https://doi.org/10.3390/pr13092959

Copyright: © 2025 by the authors. Licensee MDPI, Basel, Switzerland. This article is an open access article distributed under the terms and conditions of the Creative Commons Attribution (CC BY) license (https://creativecommons.org/licenses/by/4.0/).

1. Introduction

In recent years, against the backdrop of the in-depth implementation of China's national "14th Five-Year" strategic plan, the construction of transportation infrastructure in the country has shown a distinct westward expansion trend. The special geological conditions in western regions have posed unprecedented technical challenges to tunnel construction. To address these challenges, tunnel construction is developing towards deeper burial, larger cross-sections, and extended lengths [1]. With the annual expansion of tunnel construction scale in China, there has been a qualitative leap and leapfrog development in tunnel engineering technology. Through continuous technological innovation and accumulated engineering practices, China has become one of the world's powerful nations in tunnel construction. In the context of drill-and-blast construction combined with trackless transportation, air purification in tunnels relies entirely on mechanical ventilation systems. The efficiency of the ventilation system configuration directly determines the progress and quality of the overall project [2]. In particular, dust, CO, and other pollutants generated

during key processes such as drilling, blasting, shotcrete, and slag removal constitute the main environmental risk sources at the construction site [3]. These particulate pollutants not only threaten construction safety but also cause serious occupational health hazards to workers [4].

In international research on dust migration characteristics, the migration behavior of particulate matter is mainly affected by its particle size distribution, mass characteristics, and inertial effects during movement. Some scholars have found that the law of dust migration is related to the size, mass, and inertial force of dust. Rahimi et al. [5] identified the key parameters affecting pollutant diffusion based on uncertainty analysis methods. They used the Monte Carlo Simulation (MCS) method to conduct probabilistic prediction on the temporal and spatial evolution laws of gaseous pollutants. Nie et al. [6] used numerical simulation to obtain the coupled diffusion law of airflow–gas–dust during roadway excavation under long-pressure short-suction ventilation conditions and determined the optimal distance of the exhaust duct from the working face. Liu et al. [7] studied the characteristics of respirable dust and particle size distribution of tunneling dust through field experiments. Combined with Fluent numerical simulation, they further explored the axial and radial diffusion laws of dust in the air field and the upper and lower parts of the tunnel face. Chen et al. [8] conducted on-site measurements and numerical simulations in railway tunnels. A dust meter was used to monitor the on-site dust level every 10 s. Based on the theory of turbulent diffusion, a relationship between dust concentration and spatiotemporal variables was established. Numerical simulations of three stages (shock wave generation, pre-ventilation, and post-ventilation) were carried out using on-site dust monitoring data and dust characteristics. Wang et al. [9] constructed a multi-factor collaborative dust suppression model to analyze the dust control effect in mine tunnels. A comprehensive numerical model of dynamic tunneling operations, conveyor belt operation, spray dust suppression, water curtain purification, and flow guiding devices was established using CFD to verify the effectiveness of combined measures. Xu et al. [10] constructed a numerical model of dust diffusion and used response surface methodology to evaluate the interactive effects of key parameters. The tunnel model was validated for reliability based on on-site monitoring, and the Box–Behnken Design (BBD) method was used to explore the coupling mechanism between various factors. Liu et al. [11] used Fluent numerical simulation to reveal the flow field characteristics and dust migration laws under forced ventilation. The results showed that the wind speed at the center of the vortex zone is lower than that in the surrounding area, and the distribution along the path shows a decreasing trend, eventually stabilizing at 0.5 m/s. The dust mass concentration on the return air side of the tunnel is higher than that on the air duct side, and reducing the distance from the air outlet to the tunneling face and increasing the wind speed can improve the dust removal effect. Zhou et al. [12] evaluated the basic characteristics and pollution characteristics of dust from different lithologies in the mine environment, studied the spatiotemporal evolution law of rock-containing dust using Fluent, and analyzed the influence of rock-containing dust on water mist dust suppression characteristics.

At present, research on ventilation and dust removal measures is mainly focused on mining roadway excavation faces. For dust pollution control, five types of measures are generally adopted: source containment, sedimentation promotion, concentration reduction, effective removal, and combined dust removal. Xie Zhuwei [13] studied the dust characteristics and control mechanisms in tunnel construction based on on-site monitoring and numerical simulation. A gas–dust–liquid three-phase interaction model was constructed using the CFD-DEM coupling method to optimize the synergy between the ventilation system and spray devices. The results showed that reasonable air supply outlet positions and spray parameters can improve dust removal efficiency, and low-pressure spray shows good

practicality under specific working conditions. Liu Haijun et al. [14] achieved the optimal balance between air quality and energy efficiency in tunnel construction environments based on equipment optimization configuration and intelligent management and control strategies. A comprehensive management scheme combining scientific selection, technical improvement, and intelligent regulation can improve the dust control effect in tunnels. Xue Yongqing [15], relying on the TBM construction section of the Qinling Tunnel, explored the influence of ventilation parameters on tunnel dust reduction using numerical simulation and on-site monitoring. The results showed that the dust concentration decreases with the increase in distance from the tunnel face, and high wind speed can effectively control the dust concentration in the working area. When the air supply duct is 15 m away from the tunnel face, the dust concentration in the concentrated area of construction workers is controlled below the standard limit. Hu Yaozhou [16] used on-site tests and numerical simulation to explore the application effect of negative ion technology in tunnel dust removal, revealing the synergistic effect of diffusion charging and field-induced charging. The results showed that the negative ion purification system improves the removal efficiency of total dust, PM10, and PM2.5 by 22–40%, and the contribution rate of diffusion charging to 0.1–0.5 μm particles can reach 50–90%. Yin et al. [17] conducted research on the dust removal efficiency of wall-attached air ducts in mines under pressure-suction collaboration, obtained the optimal parameters for ventilation and dust reduction, and established a quantitative relationship between ventilation parameters and dust removal efficiency. Nie et al. [18] studied the dust control effect of the pressure-exhaust combined ventilation mode at the excavation face, and the results showed that the optimal dust removal effect can be obtained when the exhaust air volume is 250 m^3/min and the pressure air volume is 150 m^3/min. Wang et al. [19] studied the droplet size distribution characteristics and their spatial diffusion laws within the spray pressure range of 0.5–4 MPa, and developed spray dust removal equipment suitable for tunnel excavation faces. Sun Zhongqiang [20] conducted experimental research on spray dust reduction in highway tunnel drill-and-blast construction, and the results showed that under specific working conditions, the droplet size is negatively correlated with the supply air pressure, which helps to enhance the inertial collision effect between dust particles and droplets and improve dust removal efficiency.

2. Project Overview

This paper is based on the Zimuyan Tunnel project, a component of the Daozhen-Wulong Expressway. The project is situated in Luolong Town, Daozhen County, Guizhou Province, within the northern region of the Qianbei Plateau. The tunnel is a separated twin-tube four-lane extra-long tunnel with a total length of 7407.5 m and a maximum overburden depth of approximately 695 m. It is constructed using the full-face drilling and blasting method, with an excavated cross-sectional area of 102.87 m^2. The explosive consumption is typically between 270 and 300 kg per cycle, with the left and right bores each completing two cycles every 24 h. Transportation is facilitated by diesel-powered, trackless vehicles. The tunnel features a clear width of 10.25 m and a clear height of 5.0 m, with its specific location and section dimensions shown in Figure 1. Both tubes have a single-sided slope, with a longitudinal grade of 1.75% for the left tube and 1.77% for the right tube. The tunnel alignment primarily traverses the central gorge region of the South Qinling Mountains, an area characterized by significant topographic relief, with elevations ranging from 775 m to 914 m and a relative elevation difference of approximately 139 m. A vertical shaft, 428.208 m in depth with an excavated diameter of 7.6 m, is located 40 m to the right of the right-hand tunnel at station YK40+021 (facing in the direction of increasing mileage). Forced draft ventilation is employed in both tubes, supplying fresh air to the

working face while displacing contaminated air. Each portal is equipped with a 2 × 160 kW SFB energy-saving axial flow fan connected to a 1.8 m diameter flexible duct.

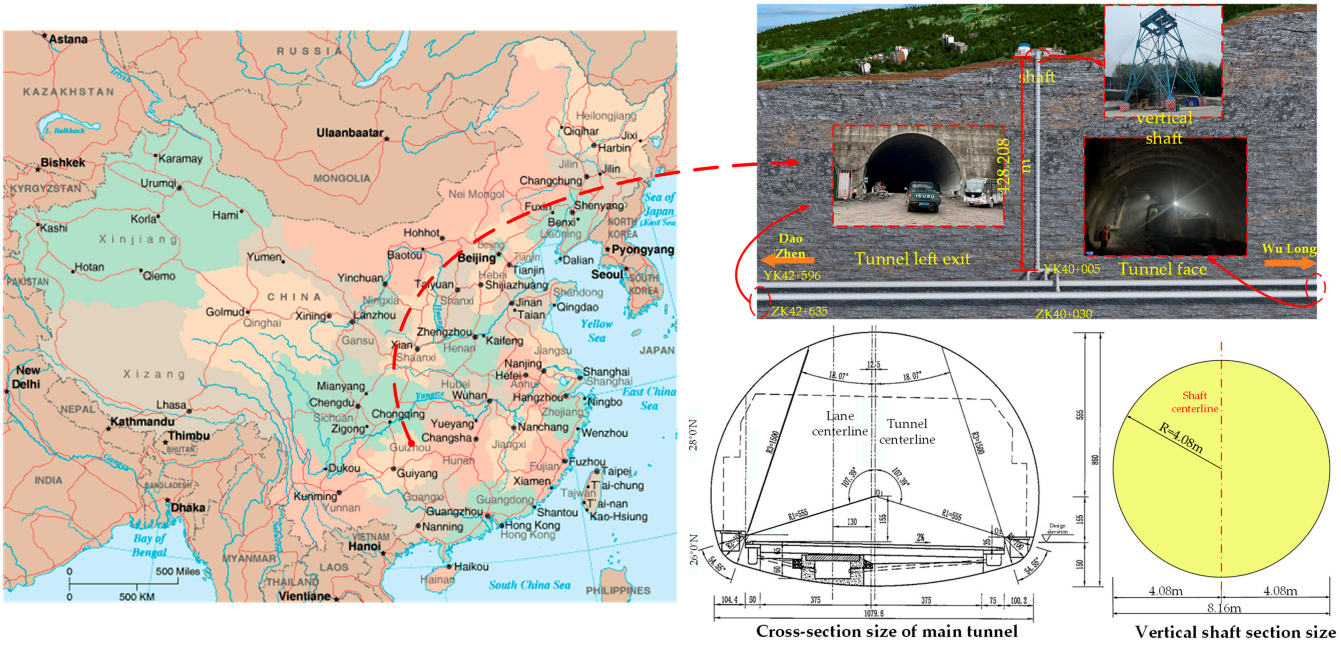

Figure 1. Tunnel location and section size.

3. Numerical Simulation of Dust Transport Characteristics During Tunnel Blasting Construction

3.1. Model Establishment and Mesh Generation

A dynamic simulation of the Zimuyan Tunnel's construction ventilation process was conducted, with the model developed based on the actual engineering progress, modeling is shown in Figure 2. The 3D model was meshed using ICEM CFD. To account for the relative complexity of the cross-passage locations and to reduce computational cost, a hybrid meshing strategy was adopted. The main tunnel sections were discretized with a structured hexahedral mesh, while the connecting passages were modeled using an unstructured tetrahedral mesh. These meshes were then coupled to ensure the accuracy of the airflow simulation. Local mesh refinement was applied at the surface of the air duct outlet. The overall mesh quality was maintained above 0.6 [21], resulting in a total mesh count of 2,473,190 cells.

A mesh independence study was conducted to evaluate the effect of mesh density on the computational results while considering computational cost. Five different unit mesh sizes—0.2, 0.4, 0.6, 0.8 and 1.0—were used to create five grids, designated Grid_A, Grid_B, Grid_C, Grid_D, and Grid_E, respectively. The total cell counts for these grids were: Grid_A: 468,978; Grid_B: 316,069; Grid_C: 247,828; Grid_D: 188,433; and Grid_E: 154,312. The air velocity within the tunnel was monitored for each case. As shown in Figure 3, a comparative analysis of the results revealed that Grid_A, Grid_B, and Grid_C exhibited a converging trend. Based on a comprehensive evaluation of accuracy and computational efficiency, Grid_C, with a unit mesh size of 0.6, was selected as the standard for meshing.

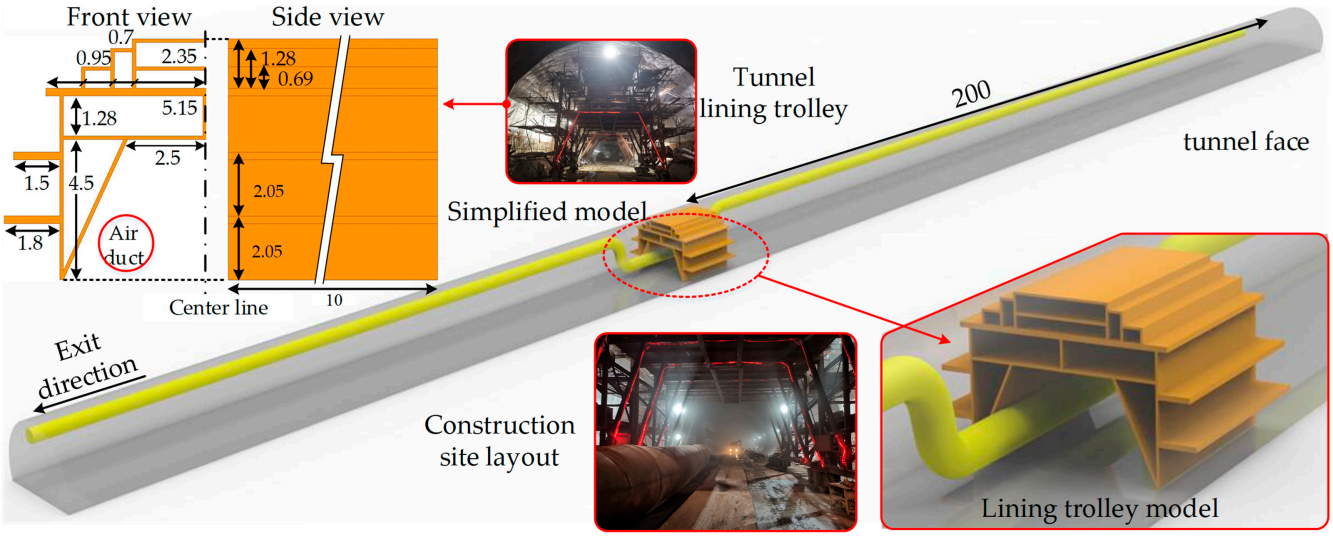

Figure 2. Three-dimensional modeling trolley segment (m).

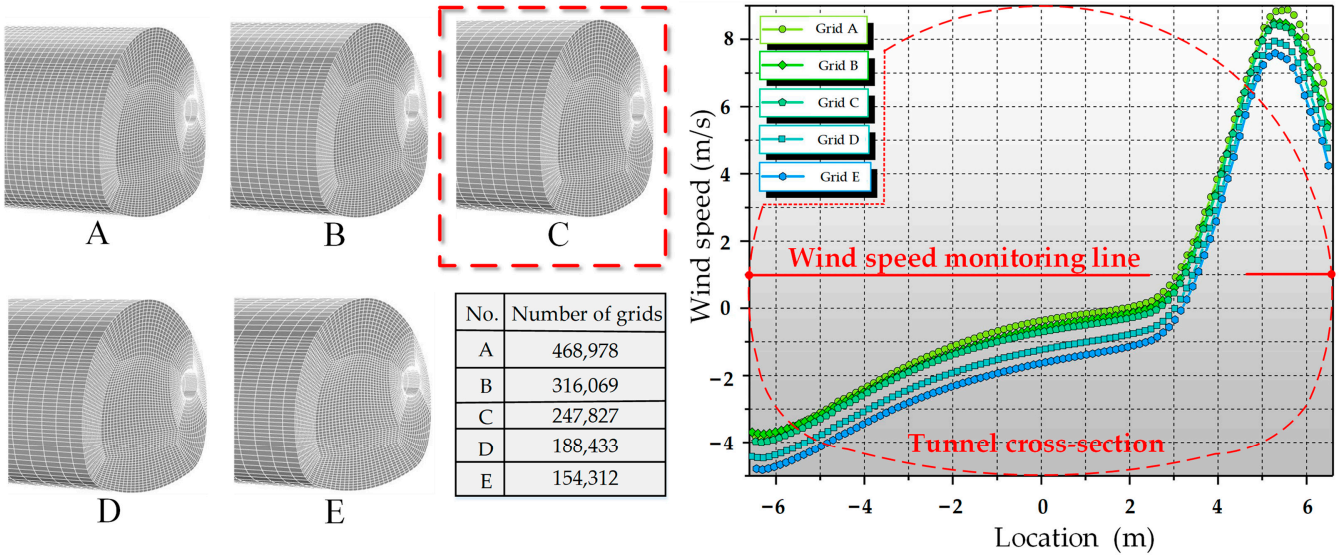

No.	Number of grids
A	468,978
B	316,069
C	247,827
D	188,433
E	154,312

Figure 3. Mesh independence.

3.2. Boundary Conditions and Key Solver Settings

During a tunnel construction cycle, pollutant dispersion is influenced by numerous factors, consequently, the simulation parameters and boundary conditions cannot perfectly replicate the actual field conditions. Based on a preliminary analysis of the tunnel environment, a pressure-based transient solver was selected, and the SIMPLE algorithm was employed for the pressure-velocity coupling scheme. The standard k-ε two-equation model was chosen for turbulence modeling. A second-order implicit scheme was applied for the discretization of the momentum, energy, turbulent kinetic energy (k), and turbulence dissipation rate (ε) equations. The ventilation fan was defined as a velocity inlet boundary condition. The tunnel portal was set as a pressure outlet boundary with zero gauge pressure. The pressure gradient normal to the wall surfaces was also set to zero. A dust release source was established at the blasting face to conduct a transient numerical simulation of gas–solid two-phase flow. The key parameters for the discrete phase model (DPM) employed in this simulation are presented in Table 1.

Table 1. Discrete phase model parameter settings.

Parameter Type	Parameter Settings	Settings
Computational dust model	time	Unsteady
	DPM	On
	Viscous model	k-ε model
Discrete phase parameters	Interaction with the continuous phase	On
	Number of Continuous Phase Iteration Per DPM iteration	On
	Update DPM Sources Every FlowIteration	On
	Unsteady Particle Tracking	On
	Time Scale Constant	0.01
	Max Number of Steps	20,000

Prior to performing the discrete phase numerical calculations, the dust parameters must be defined. The dust mass flow rate is determined using the following formula to calculate the quantity of dust per unit time, which is then used in conjunction with the blasting operation to estimate the total dust generation.

$$Q_d = q_d \times A \times v_d = 500\ \mathrm{mg/m^3} \times 138 \times 10 = 0.69\ \mathrm{kg/s}$$

where Q_d is the mass flow rate (kg/s); q is the dust concentration at the source, assumed to be 500 mg/m^3; A is the cross-sectional area of the tunnel face (138 m^2); The dust from the blast is considered to be generated instantaneously over a set duration of 1 s, resulting in a total dust mass of 0.69 kg. The classification of dust particles is given in Table 2. Particles with a diameter below 7 μm can readily enter the human respiratory system and cause harm. Dust with a diameter smaller than 2 μm is particularly hazardous to human health due to its strong tendency to remain suspended in the air. For this study, the simulated dust particle size distribution was set from 1 to 60 μm, with calculations performed using a mean diameter of 11 μm.

Table 2. Characteristics of different dust particle sizes.

Particle Type	Particle Size	Characteristics of Dust
Coarse particles	>40 μm	Settle rapidly in the air
Fine particles	10–40 μm	Visible to the naked eye in bright environments
Micron particles	0.25–10 μm	Observable only with an optical microscope
Submicron particles	≤0.25 μm	Recognizable solely through an electron microscope

The dispersion characteristics of dust directly influence its suspension properties within the tunnel. When dispersibility increases, dust particles are more apt to remain suspended, which extends their residence time in the air and consequently increases the probability of being inhaled by workers. The widely accepted Rosin-Rammler distribution function was used in the simulation to model the particle size distribution. The specific parameters for the blasting dust and injection source used in the calculations are detailed in Table 3.

In the numerical simulation, when dust particles interact with the boundaries of the computational domain, their behavior is defined by one of the following three conditions:

Trap: The particle is captured upon contacting the boundary, representing deposition, and its trajectory calculation is terminated.

Escape: The particle passes through the boundary, exiting the computational domain, and its calculation is subsequently terminated.

Reflect: The particle bounces off the boundary and continues to move within the domain until it reaches the predefined maximum number of calculation steps or another termination condition is met.

The specific boundary conditions set for the various tunnel surfaces are provided in Table 3.

Table 3. Settings for Dust Injection Source Parameters and Tunnel Wall Boundary Conditions.

Injection	Setting Status	Boundary	Model Setup
Injection Type	Surface	Outlet	Escape
Material	Dolomite		
Diameter Distribution	R-R distribution	Wall DPM Conditon	Trap
Min. Diameter	1×10^{-6} m		
Max. Diameter	60×10^{-6} m		
Mean. Diameter	11×10^{-6} m	Wall Shear Conditon	No Slip
Spread Parameter	1.9		
Total Flow Rate	0.5 kg/s	Wall Boundary	Reflect
Turbulent Dispersion	Stochastic Tracking		
Drag Law	Spherical	Wall Roughness Constant	0.5
Number of Tries	1000		
Time Scale Constant	0.15		

3.3. Validation of the Numerical Model Based on Field Measurements

3.3.1. Field Testing

Evaluate the effectiveness and integrity of the ventilation system, optimize construction environment control strategies, maintain safety during in-tunnel construction, and protect the health of construction personnel, real-time air quality monitoring was conducted for the ventilation conditions at the working face section of the Zimuyan Tunnel.

For on-site wind speed measurement, a Testo 405i thermal anemometer (Testo SE & Co. KGaA, Titisee-Neustadt, Germany) was used. Wireless data synchronization was established via Bluetooth 5.0, connecting the anemometer's numerical display unit to its sensor. The sensor's axis was aligned parallel to the longitudinal axis of the tunnel, ensuring the angle of incidence deviation was less than 3°. To ensure the accuracy of the monitoring data, the device was kept in a vertical c, allowing airflow to travel along the sensor's axis to accurately measure the longitudinal return air velocity within the tunnel. The wind speed signal was monitored continuously for 120 s. Measurements began once the anemometer readings started fluctuating with the airflow. During this process, the steady-state wind speed was extracted after the data on the display unit stabilized, and a relatively stable reading was selected as the final measurement value. After completing one measurement, the anemometer was moved to the next test point to repeat the procedure, and the data was recorded synchronously.

For dust concentration monitoring using a CCZ-1000 direct-reading dust meter (Qingdao Laoshan Electronic Instrument General Factory Co., Ltd., Qingdao, China), monitoring personnel first arrived at the predetermined measurement points, installed support brackets, and assembled the components of the instrument and the dust collection device. During assembly, the sensor's orientation had to be adjusted to be perpendicular to the trajectory of dust movement. The filter membrane was set in advance according to on-site needs, the monitoring was initiated with a preset time interval, and the real-time on-site monitoring process began. After one monitoring cycle was complete, the data

was immediately recorded, and the filter membrane was quickly replaced to seamlessly transition to the next round of monitoring.

For CO concentration monitoring, monitoring personnel carried an EM-20 carbon monoxide sensor (China Coal Technology and Engineering Group Chongqing Research Institute Co., Ltd., Chongqing, China) to the predetermined measurement points. The probe was held perpendicular to the direction of the longitudinal airflow to ensure measurement accuracy, while data was observed on a real-time display and collected by recording personnel as required. For dust concentration monitoring, personnel set up horizontal brackets at the designated points in advance, assembled the main instrument body and the dust collection device, kept the sensor perpendicular to the dust flow direction, installed the filter membrane, set the monitoring time interval as required to begin monitoring, and after completion, recorded the data and quickly replaced the filter membrane to start the next monitoring cycle.

The in-tunnel monitoring equipment and process are illustrated in Table 4 and Figure 4.

Table 4. Measuring instruments and key technical parameters.

Test Item	Instruments	Key Technical Parameters	
		Measurement Range	Accuracy
Dust Concentration	CCZ-1000 direct-reading dust meter	0–1000 mg/m^3	<0.1
Wind Speed	Testo 405i thermal anemometer	0–20 m/s	0.03
CO	EM-20 carbon monoxide sensor	0–2000 ppm	1

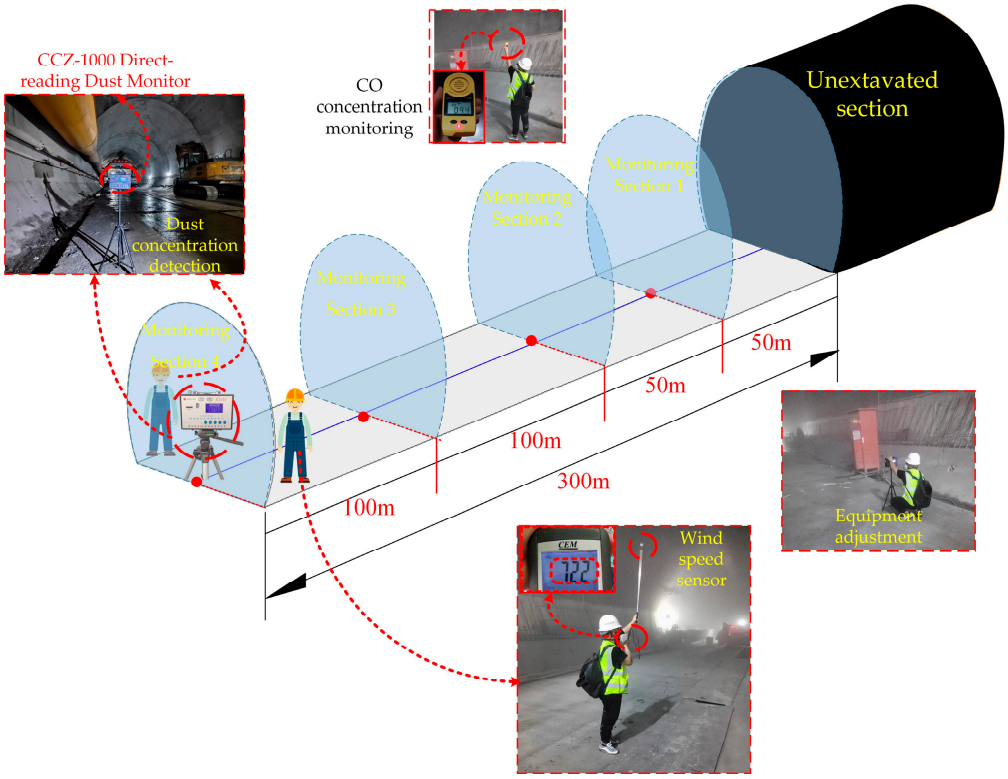

Figure 4. Usage process of various monitoring devices.

3.3.2. Model Validation

To verify the accuracy of the model, a comparison was made between the numerically simulated data and the on-site measured data of cross-sectional wind speed and dust concentration. The on-site monitoring data from the working face area of the Zimuyan

Tunnel were taken as the measured results. For the numerical simulation, after 30 min of continuous ventilation, the cross-sectional wind speed and dust concentration in the monitoring section were extracted. The measured results were compared with the numerical simulation results, and verification was conducted through relative deviation analysis. The comparison between the on-site monitoring data and the simulated data is shown in Figure 5. It can be seen that the numerical simulation results are basically consistent with the measured values, with similar distribution patterns. The maximum deviation of wind speed is 16%, and the maximum deviation of dust concentration is 16.6%. The model calculations are consistent with the actual on-site conditions, so this model can be used for further in-depth analysis.

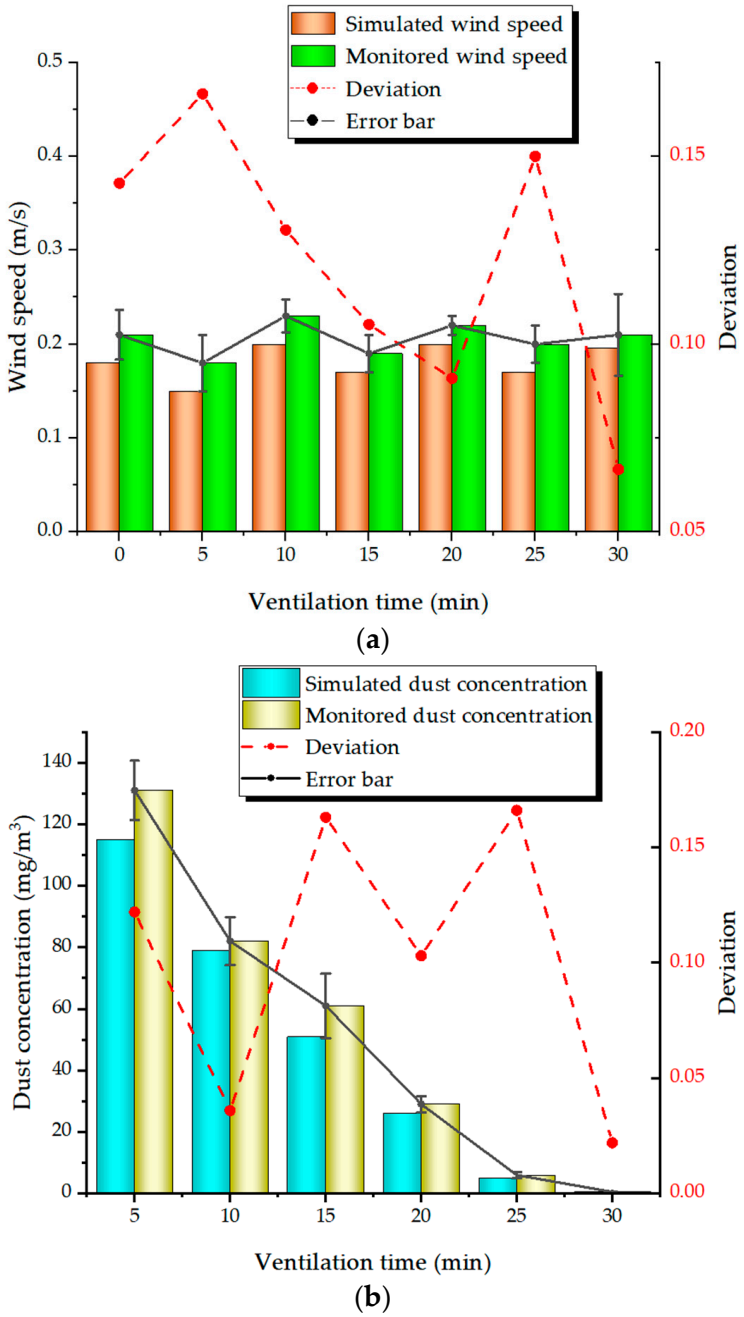

Figure 5. Verification of comparison results between simulation and on-site monitoring. (**a**) Comparison chart of wind speed. (**b**) Comparison chart of dust concentration.

3.4. Airflow Field and Dust Transport Characteristics Under Single-End Tunneling

3.4.1. Distribution Characteristics of the Airflow Field and the Mechanism of Pressure Difference

After a tunnel blast, the construction ventilation system is activated. Fresh air is forced from the axial flow fan outside the portal through the duct to the working face. Pollutants such as blasting dust and CO are discharged out of the tunnel with the airflow. As the driving force for pollutant migration and dispersion, the distribution and trajectory of the airflow play a crucial role in pollutant transport. As the distance from the working face increases, the airflow field tends to stabilize, and its effect on driving pollutants becomes more singular. Taking the 200 m working section under single-end excavation as the research object, the structure and distribution characteristics of the stable airflow field are discussed. Figure 6 shows the spatial distribution cloud map of the stable airflow field under single-end excavation. It can be seen that the spatial distribution characteristics of the airflow field can be divided into three stages based on the distance from the working face: Within the range of 0–30 m, the airflow field undergoes significant changes. The airflow advances from the duct outlet in a jet-like form. Obstructed by the working face, the airflow jet deflects towards the left side of the face, adhering to the wall. After being blocked by the left tunnel wall, it rebounds a certain distance towards the right tunnel wall and then gradually diffuses outward, forming an annular vortex at the center of this section. In the 30–60 m range, the airflow field gradually moves towards the tunnel centerline. The original jet-like distribution begins to diverge outwards. The air velocity at the tunnel crown is significantly higher than that at the tunnel floor, which is unfavorable for pollutant removal in actual engineering. In the 60–200 m range, the jet-like form of the airflow has basically disappeared, and it gradually decreases along the longitudinal direction while maintaining a relatively stable overall form.

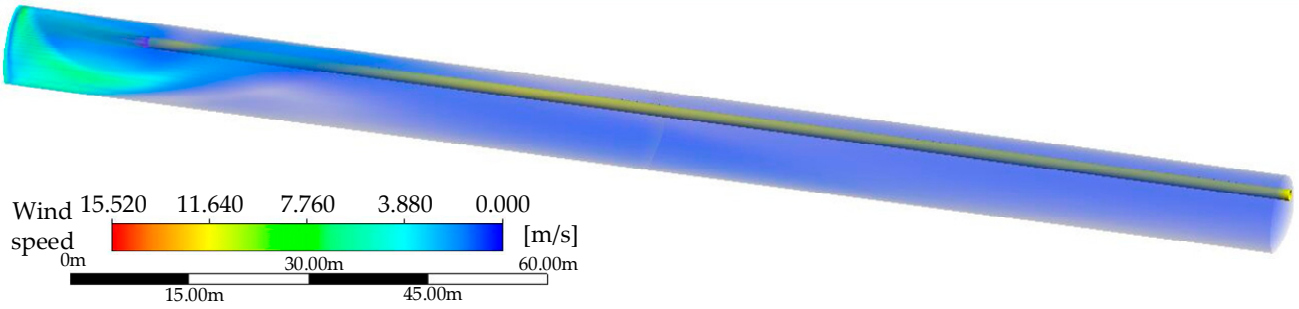

Figure 6. Three-dimensional air velocity contour map within 200 m of the face after stabilization of the airflow field.

To further observe this trend, an X-Y wind speed cloud map at Z = 3 m within a 200 m range from the working face was extracted, as shown in Figure 7. It can be seen that after the high-velocity jet hits the working face, it flows towards the side opposite the duct in a right-angled, wall-adhering form. Upon reaching the left wall, it spreads out in a quasi-circular pattern, with a significant drop in the central air velocity. The return air velocity is high in the approximately 15 m section from the duct outlet to the working face, reaching about 7.76 m/s. However, a vortex forms about 2 m from the working face, where the air velocity at the vortex center is very low, close to 0 m/s. This can easily lead to local pollutant accumulation or circulation only within the working face area, preventing it from being discharged outwards.

To investigate the formation mechanism of the airflow vortex, the pressure exerted by the airflow on the working face was analyzed based on the principle of force interaction, as shown in Figure 8. At 30 s of ventilation, the pressure on the upper right side of

the working face is the highest, about 15 Pa, and it gradually decreases towards the left side, with a minimum of about 3 Pa, then gradually recovers near the left wall. It can be seen that the airflow field near the working face is unstable at this time, with no obvious vortex, and the pressure difference on the face is not significant. After 90 s of ventilation, a clear stratification of pressure appears on the working face. A distinct high-pressure zone emerges at the position opposite the duct outlet on the right side of the face, with a maximum value of about 37.67 Pa, which gradually decreases in a circular pattern outwards, with the overall range being 37.67~26.322 Pa. The pressure on the central part of the face is lower, until the pressure on the left side gradually increases. This shows that the left and right walls of the working face have a significant obstructing effect on the airflow, and after multiple rebounds, a vortex eventually forms near the working face.

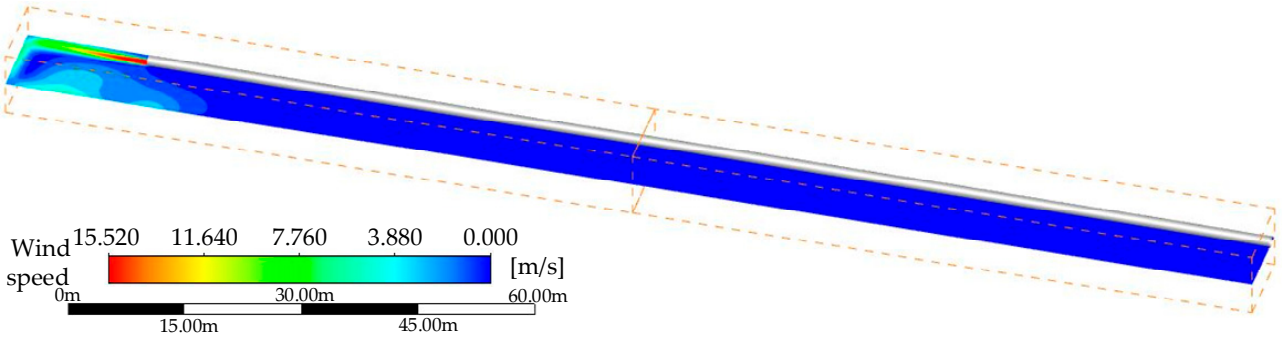

Figure 7. Air velocity contour map of the X-Y Cross-Section at 200 m from the face after stabilization of the airflow field.

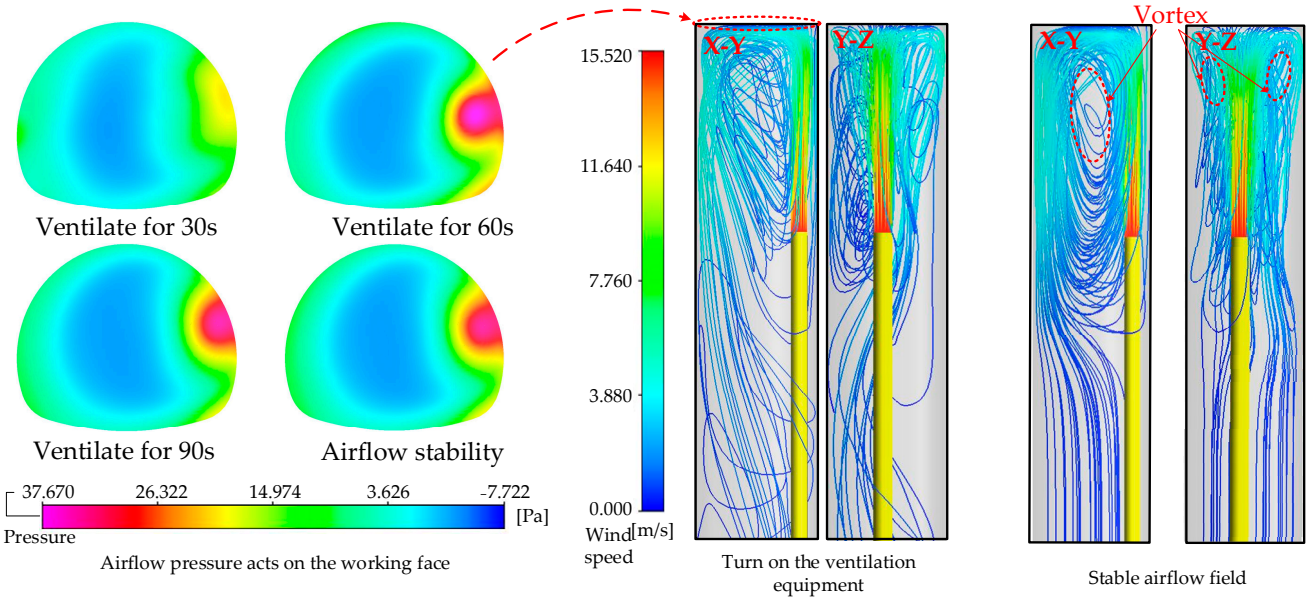

Figure 8. Analysis of airflow field and air pressure within the local scope of the face.

3.4.2. Spatiotemporal Distribution Characteristics and Transport Patterns of Dust

Blasting dust has a certain mass and is affected by gravitational acceleration. At the same time, volume collisions occur between particles of different sizes under the coupling effect of the airflow. Its diffusion mechanism and characteristic patterns are different from those of harmful gaseous pollutants in the tunnel. Taking the initial dust field as the research object, its coupling effect with the airflow field is explored. Figure 9 is a schematic diagram of dust diffusion under the coupling effect of the airflow field. Influenced by the high-velocity airflow near the working face, the blasting dust is pushed outwards as

a whole from its initial clustered state in a short period, exhibiting a flow characteristic of "overall outward movement, local diffusion." Under the coupling effect of the airflow, the blasting dust begins to migrate towards the end far from the duct, influenced by the airflow from the duct arranged on the right side of the tunnel. Some dust settles locally, and then diffuses upwards at a certain inclination angle. At this time, the dust still maintains a certain degree of aggregation. There is a difference in the distribution of larger and smaller particles. Due to the influence of environmental gravitational acceleration, heavier particles (i.e., those with larger diameters) are distributed lower vertically than lighter particles. After 10 s of ventilation, a clear stratification phenomenon based on particle size distribution can be observed.

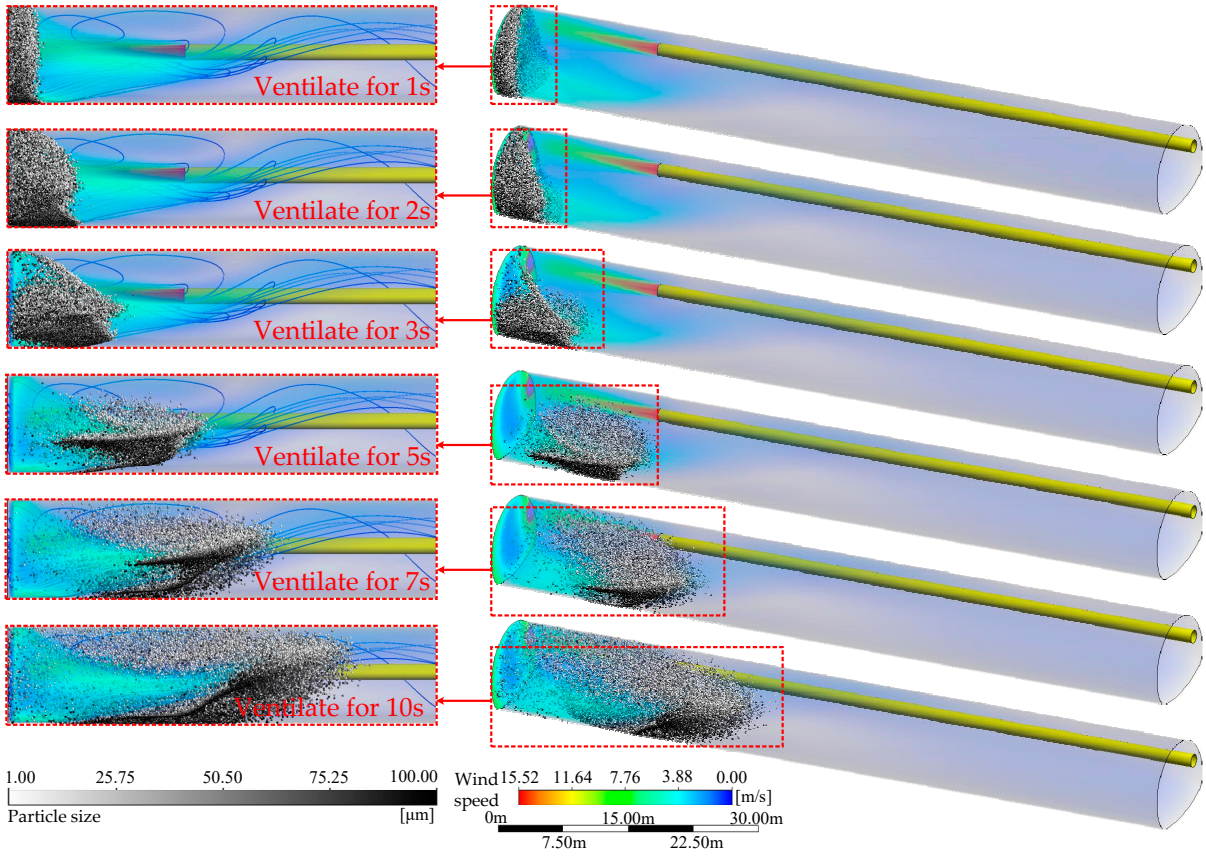

Figure 9. Dust diffusion under the coupling effect of airflow field.

Figure 10 shows the dust transport cloud map within 30 min of ventilation. It can be seen that within 300 s, the blasting dust begins to diffuse and disperse from a clustered form. As time increases, the overall volume concentration of the dust begins to decrease, becoming diluted and attenuated, and gradually filling the entire 200 m construction section. After 300 s of ventilation, the dust concentration gradually decreases. At 600 s, the number of suspended dust particles in the tunnel decreases sharply, and some larger dust particles that were not discharged from the working face section settle at the bottom of the tunnel. At 1800 s, the dust within the 200 m range of the working face is basically cleared from this section, with some heavier particles settling near the cross-section or at the end of this section.

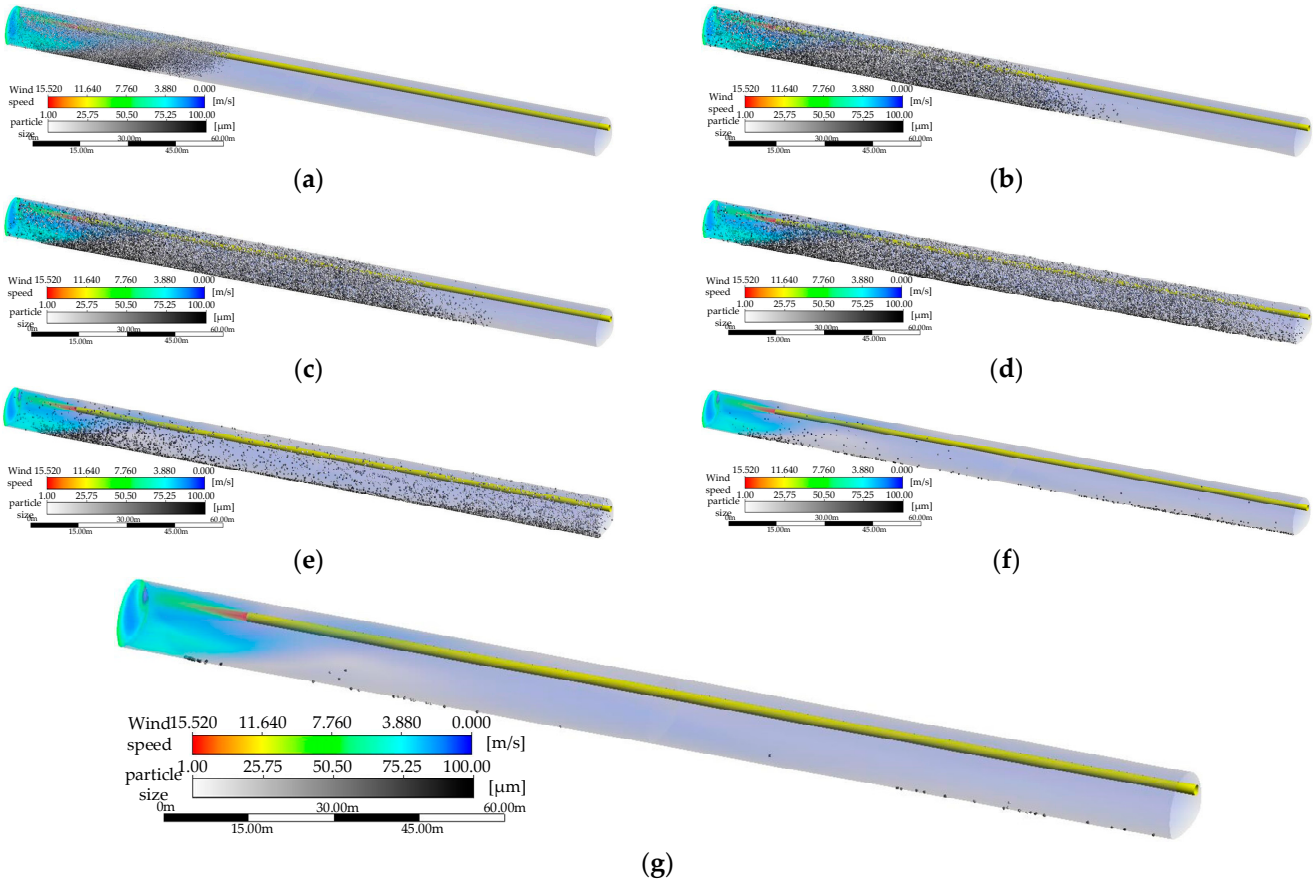

Figure 10. Schematic diagram of temporal distribution of dust within 30 min of ventilation. (**a**) Dust distribution within 30 s of ventilation. (**b**) Dust distribution within 120 s of ventilation. (**c**) Dust distribution within 180 s of ventilation. (**d**) Dust distribution within 300 s of ventilation. (**e**) Dust distribution within 600 s of ventilation. (**f**) Dust distribution within 1200 s of ventilation. (**g**) Dust distribution map within 1800 s of ventilation.

4. Model Experiment Study on Water Mist Dust Suppression Schemes at the Working Face

4.1. Model Experiment Setup

A physical model of the Zimuyan Tunnel was constructed at a 1:20 scale relative to the actual tunnel cross-section. To allow for more intuitive observation of pollutant transport and the in-tunnel environment, the model was custom-built using 3 mm thick transparent acrylic sheets. The model comprised 9 sections, creating a total length of 14 m. Each section measured 1.5 m in length, except for the 0.5 m section representing the working face. The entire assembly was supported by small tables at a height of 0.55 m above the ground. In addition to mechanical connectors, the joints between sections were sealed with aluminum foil tape. To realistically simulate the in-tunnel environment, toy vehicles and a simplified model of a lining trolley were placed inside. The lining trolley was positioned approximately 6.5 m from the working face, corresponding to a scaled distance of 130 m in the actual tunnel. An SE-A10S variable frequency mixed-flow ducted fan was used for the experiment. To account for on-site air leakage, a 10 cm inner-diameter Oxford cloth duct was chosen to model the 2 m diameter duct used in the field, thereby maximizing the replication of site conditions. After connecting the fan and duct, the maximum air velocity at the outlet reached 2 m/s. A constant pressure funnel was used as the dust generation device; its constant pressure mechanism effectively prevents blockages caused

by pressure variations during dust release, ensuring the smooth execution of the experiment. A schematic diagram of the model structure is shown in Figure 11.



Figure 11. Schematic diagram of the tunnel model.

4.2. Experimental Procedure and Working Condition Settings

4.2.1. Working Condition Settings

The experiment primarily focused on the water mist spray nozzle angle and nozzle flow rate to measure the spatiotemporal distribution of dust in the tunnel under different nozzle angles and flow rates. The aim was to explore the key factors affecting the efficiency of water mist dust suppression during the construction of extra-long tunnels, thereby providing a reference for engineering practice. Considering that in actual tunnel construction, the initial dust concentration after blasting can vary greatly due to factors such as geological conditions, construction environment, and the type and amount of explosives, the initial dust concentration in this study was set to 400 mg/m^3 for all cases to maximize the investigation of factors affecting water mist dust suppression efficiency. The nozzle angle was based on the tunnel centerline at the crown, with 90° being vertically downwards. Five working conditions were set: −30°, −60°, 90°, 60°, and 30°, where the negative sign indicates the direction towards the working face. The nozzle flow rate is related to the nozzle model and manufacturer. The nozzle orifice used in the experiment was 0.5 mm, with a spray diameter of about 60 mm and a spray flow rate of 0.03–0.08 L/min. Therefore, three flow rate conditions were set: 0.03 L/min, 0.06 L/min, and 0.08 L/min. The specific experimental conditions are shown in Table 5.

Table 5. Operating conditions settings.

Condition	Nozzle Angle (°)	Nozzle Flow (L/min)	Init. Dust Conc. (mg/m^3)
1-1	−30	0.06	400
1-2	−60		
1-3	90		
1-4	60		
1-5	30		
2-1	90	0.03	
2-2		0.06	
2-3		0.08	

4.2.2. Monitoring Cross-Section and Point Setup

To best demonstrate the effect of the water mist dust suppression device and to investigate the spatiotemporal distribution of dust under different conditions, the experiment focused on monitoring the in-tunnel wind speed and dust concentration. Three monitoring sections were set up: 1 m in front of the water mist dust suppression device (i.e., at the duct outlet, corresponding to the device being placed at an actual distance of 20 m from the duct outlet), at the location of the water mist device, and 1 m behind the water mist device (corresponding to an actual distance of 20 m). The specific monitoring points are shown in Figure 12. A PD410H-M5RF660CY wind speed transmitter (The manufacturer is Shunlaida, Jiangyin City, China)was used for wind speed monitoring, with a measurement range of 0–5 m/s. An insertion-type dust detector was used for dust monitoring, with a measurement range of 0–500 mg/m^3.

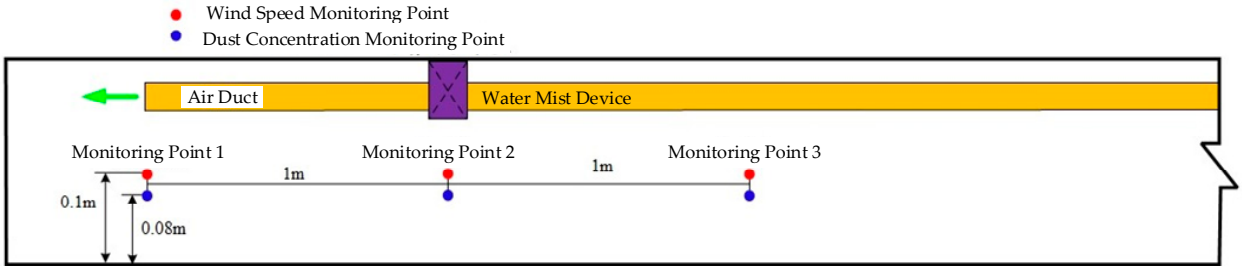

Figure 12. Layout of monitoring sections and monitoring points.

4.2.3. Experimental Procedure

The sieved and graded experimental dust was placed in the funnel, and the valve was opened. When the dust concentration at the working face reached the set value, the fan was turned on for ventilation, and the water mist dust suppression device was activated. The ventilation time was 900 s, and monitoring data was recorded every 20 s. The experimental data was collected by the monitoring instruments and monitored in real-time through a conversion interface. Figure 13 shows a schematic diagram of the water mist device angle deflection and the experimental process.

4.3. Analysis of Influencing Parameters for Spray Dust Suppression

4.3.1. Influence of Different Nozzle Angles

To study the effect of different spray angles of the water mist dust suppression device on its dust removal efficiency, five sets of comparative conditions were designed with nozzle angles of −30°, −60°, 90°, 60°, and 30°, where the negative sign represents the nozzle facing the tunnel working face. The initial dust concentration was set to 400 mg/m^3, the fan was set to its highest power setting, the ambient temperature was 8–12 °C, and the atmospheric pressure was one standard atmosphere. A total of 45 data points were recorded

over 900 s of ventilation. The comparison curves of dust concentration and in-tunnel wind speed at each monitoring point are shown in Figures 14 and 15.

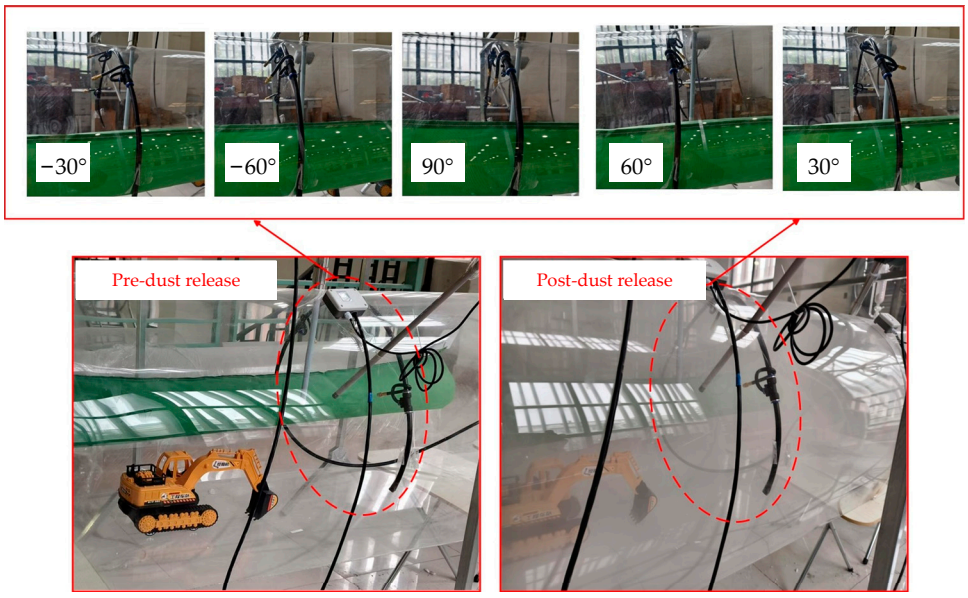

Figure 13. Test process.

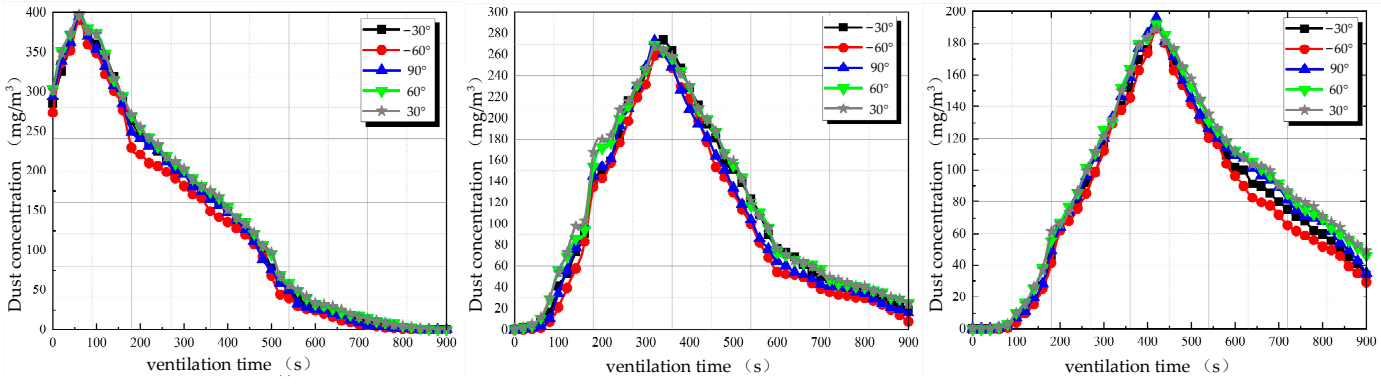

Figure 14. Comparison curve of dust concentration under different nozzle angles: (**a**) monitoring point 1; (**b**) monitoring point 2; (**c**) monitoring point 3.

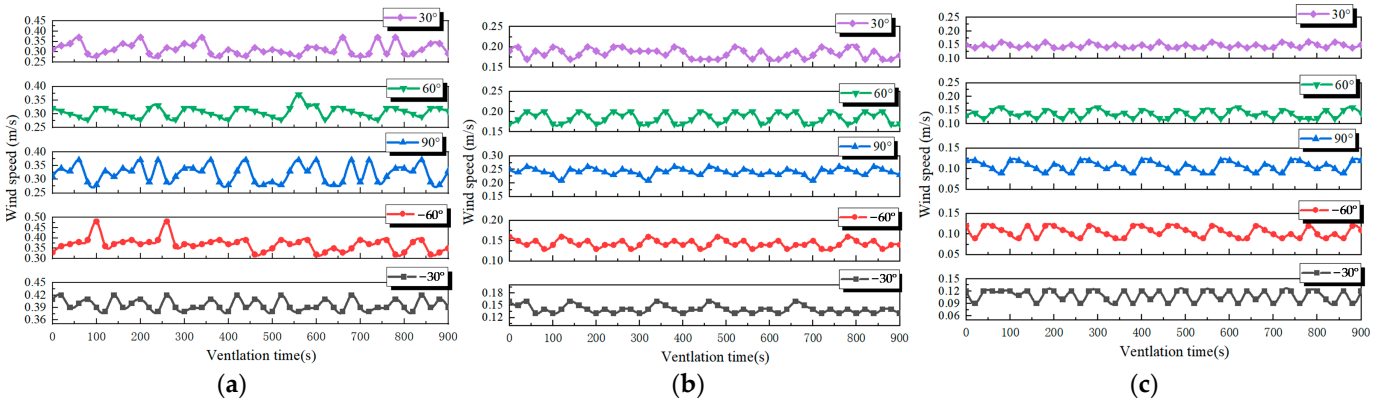

Figure 15. Comparison curve of air velocity under different nozzle angles: (**a**) monitoring point 1; (**b**) monitoring point 2; (**c**) monitoring point 3.

As shown in Figure 14, the trend of dust concentration change at the same monitoring point is basically the same for all angles, but the dust removal efficiency varies due to the

change in nozzle angle. It can be seen that the rate of decrease at each monitoring point is fastest when the nozzle angle is −60°, and slowest when the angle is 30°. At monitoring point 1, the dust concentration for the −60° condition dropped below 20 mg/m^3 (meeting construction requirements) at 620 s, while the −30°, 90°, 60°, and 30° conditions reached this threshold at 660 s, 640 s, 680 s, and 680 s, respectively. At monitoring points 2 and 3, the dust removal efficiency of the −60° condition was also relatively faster than the other conditions, showing an improvement of about 3% compared to the 90° condition. From Figure 15, it can be seen that the in-tunnel wind speed also shows differences due to the change in nozzle angle. At monitoring point 1, the maximum wind speed reached 0.41 m/s for the −30° angle, followed by −60° with an average wind speed of about 0.36 m/s. The remaining three conditions had an average speed of about 0.31 m/s. At monitoring point 2, the wind speed was highest at 90°, with a maximum of about 0.26 m/s, followed by 60° and 30° with an average speed of about 0.18 m/s. The higher speeds seen at point 1 for −30° and −60° decreased, with an average of about 0.14 m/s. At monitoring point 3, the maximum wind speed corresponded to the 30° condition, with an average speed of 0.14 m/s, followed by −60° with an average of 0.13 m/s. The remaining three conditions had an average speed of about 0.1 m/s. From the above analysis, it is clear that changing the nozzle angle has a certain impact on the tunnel's dust removal efficiency. When the nozzle faces the working face (i.e., against the dust), a certain angle adjustment can improve its efficiency. However, at the same time, the water spray from the device can interfere with the in-tunnel airflow field, affecting the wind speed. In front of the water spray, the wind speed increases due to the squeezing effect of the water flow, while behind the nozzle, the wind speed decreases due to the obstruction of the water curtain. Therefore, the nozzle angle should be adjusted moderately according to the actual site needs to improve the dust removal effect while minimizing the impact on the airflow.

4.3.2. Influence of Different Nozzle Flow Rates

To study the effect of different spray flow rates of the water mist dust suppression device on its dust removal efficiency, three sets of comparative conditions were designed with nozzle flow rates of 0.03 L/min, 0.06 L/min, and 0.08 L/min. The initial dust concentration was set to 400 mg/m^3, the fan was set to its highest power setting, the ambient temperature was 8–12 °C, and the atmospheric pressure was one standard atmosphere. A total of 45 data points were recorded over 900 s of ventilation. The comparison curves of dust concentration and in-tunnel wind speed at each monitoring point are shown in Figures 16 and 17.

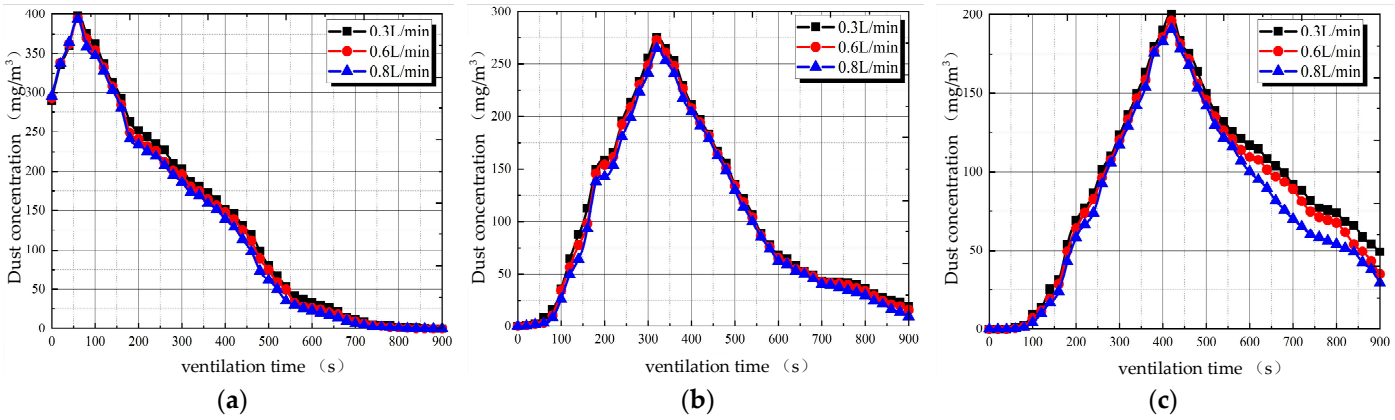

Figure 16. Comparison curve of dust concentration under different nozzle flow rates: (**a**) monitoring point 1; (**b**) monitoring point 2; (**c**) monitoring point 3.

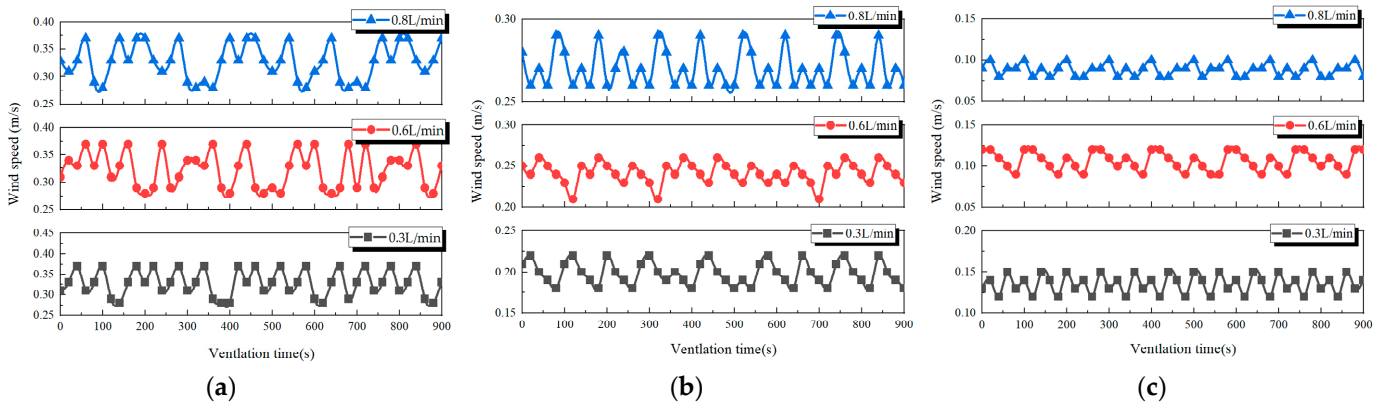

Figure 17. Comparison curve of air velocity under different nozzle flow rates: (**a**) monitoring point 1; (**b**) monitoring point 2; (**c**) monitoring point 3.

According to Figure 16, at the same monitoring point, adjusting the nozzle flow rate did not have a major impact on the trend of the dust concentration curve, but the dust removal efficiency varied. Obviously, as the nozzle flow rate increases, the dust removal efficiency rises. At monitoring point 1, increasing the nozzle flow rate shortened the time for the dust concentration to fall below the safety threshold by about 40 s. Integrating the data from all monitoring points, it can be concluded that under the experimental conditions of this study, for every 0.01 L/min increase in flow rate, the dust removal efficiency can be improved by 1–2%. From Figure 17, it can be seen that the wind speed is affected by the nozzle flow rate. At monitoring point 1, the average wind speeds for 0.03 L/min, 0.06 L/min, and 0.08 L/min were all around 0.32 m/s. At monitoring point 2, the average wind speeds were 0.19 m/s, 0.24 m/s, and 0.27 m/s, respectively. At monitoring point 3, the average wind speeds were 0.13 m/s, 0.1 m/s, and 0.08 m/s, respectively. As the flow rate of the water mist device changes, its squeezing and obstructing effects also change. When the flow rate exceeds 0.08 L/min, the local wind speed fluctuation in the tunnel exceeds 20% (affecting ventilation stability).

4.4. Discussion on Optimal Dust Removal Process Parameters

This chapter determines the optimal process conditions through scale model tests. The tests adopt the "control variable method" to isolate the influences of various parameters, and take dust removal efficiency and airflow stability as the combined evaluation criteria. The specific process is as follows:

(1) Optimal Spray Parameters: When the nozzle angle is −60° (towards the working face), the dust removal efficiency is 3% higher than that at 90° (vertically downward), and the dust removal time is shortened by 20 s;

(2) For every 0.01 L/min increase in flow rate, the dust removal efficiency increases by 1–2%. However, when the flow rate exceeds 0.08 L/min, the local wind speed fluctuation in the tunnel exceeds 20% (affecting ventilation stability), so the optimal flow rate is 0.06–0.08 L/min.

5. Conclusions

This paper analyzes the air flow field structure under the single-tunnel excavation condition of the Zimuyan Tunnel through three-dimensional numerical simulation, and clarifies the temporal and spatial distribution, migration characteristics and migration laws of dust. Combined with a 1:20 scale model test, it studies the influence of nozzle angle and flow rate of the water mist dust removal device on dust removal efficiency, clarifies the effect of these two factors on the air flow and dust migration in the tunnel, and identifies the

key influencing factors of ventilation and water mist dust removal. The main conclusions are as follows:

(1) In the initial stage of ventilation, the wind pressure on the right side of the tunnel face is relatively low, and the overall pressure difference across the tunnel face is small, with no obvious eddy current formed. In the later stage of ventilation, the air flow field stabilizes, the wind pressure on the right side of the tunnel face becomes relatively high, and the overall pressure distribution on the tunnel face shows a pressure difference gradient of "high on both sides and low in the middle". Obvious eddy currents are formed near the tunnel face. Therefore, to reduce the impact of eddy currents on the pollutant discharge efficiency of the ventilation system, efforts should be made to minimize the pressure difference gradient on the tunnel face. When the wind speed at the outlet of the air duct is constant, the theoretically calculated wind pressure on the right side of the tunnel face increases as the distance between the air duct outlet and the tunnel face decreases. Thus, the distance between the air duct outlet and the tunnel face can be appropriately adjusted to reduce the pressure difference, so as to avoid the formation of large eddy currents near the tunnel face that hinder ventilation.

(2) Affected by the high-speed air flow near the tunnel face, the blasting dust moves outward as a whole from its initial clustered state in a short time, showing the flow characteristics of "overall outward movement with local diffusion". Under the coupling effect of air flow, there is a difference in distribution between larger particles and smaller particles. Due to the influence of environmental gravitational acceleration, particles with greater mass (i.e., larger diameter) are distributed lower in the vertical direction than lighter particles. After 10 s of ventilation, an obvious stratification phenomenon based on particle size distribution can be observed.

(3) The nozzle angle and nozzle flow rate have a significant impact on the dust removal efficiency of the water mist dust removal device. With the change in nozzle angle, the efficiency of the -60° nozzle angle condition is about 3% higher than that of the 90° condition. Arranging the nozzle to face the direction of dust flow achieves better dust removal effect; however, an excessively large angle will reduce the water flow coverage range and thus affect the dust removal effect. Moreover, changing the angle will affect the air flow field in the tunnel, possibly causing an increase or decrease in wind speed in local areas, so appropriate adjustments should be made according to actual needs.

(4) The nozzle flow rate affects the dust removal effect. Under the experimental conditions of this study, for every 0.01 L/min increase in flow rate, the dust removal efficiency can be improved by 1–2%. However, as the flow rate increases, the water mist coverage range also expands, which in turn enhances the squeezing and blocking effect on the air flow in the tunnel, and the wind speed in local areas will increase more significantly. Therefore, the nozzle flow rate should be adjusted moderately according to actual needs.

Author Contributions: F.D. proposed the research plan and framework ideas for this article and completed the writing—original draft; K.R. provided financial support for the research of the project and Investigated the geological conditions and distribution of buildings and structures within the study area; G.W. provided detailed temperature parameters, highway tunnel size data and other information for this study. Y.F. processed the data collected during the construction and optimized the readability of the chart. J.Z. carried out numerical simulation after receiving the processed data, and analyzed and verified the prediction results. H.Z. optimized the organizational structure of the article and offered useful suggestions for the preparation and writing of the paper. All authors have read and agreed to the published version of the manuscript.

Funding: The study is financially supported by the Technology projects of Transportation Department of Guizhou Province (2023-122-007), and the Fundamental Research Funds for Central Universities (2682024ZTPY030, 2682023KJ001 and 2682023CX072). We are also very grateful for the National Natural Science Foundation of China (NSFC) under Grant No. 52578487.

Institutional Review Board Statement: Not applicable.

Informed Consent Statement: Not applicable.

Data Availability Statement: The original contributions presented in this study are included in the article. Further inquiries can be directed to the corresponding author(s).

Acknowledgments: We also highly appreciate the data collection and processing work of Guizhou Road and Bridge Group Co., Ltd. and Guizhou Provincial Key Laboratory of Intelligent Construction and Maintenance for Mountain Bridge-Tumnel Engineering. Finally, the author would like to thank the reviewers for their useful comments and the editors for improving the manuscript.

Conflicts of Interest: Author Fayi Deng, Kaifu Ren, Guofeng Wang and Yongqiao Fang were employed by the company Guizhou Road and Bridge Group Co., Ltd. The remaining authors declare that the research was conducted in the absence of any commercial or financial relationships that could be construed as a potential conflict of interest.

References

1. Zhao, Z.; Xu, H.; Liu, G.A. Robust numerical method for modeling ventilation through longtunnels in high temperature regions based on 1D pipe model. *Tunn. Undergr. Space Technol.* **2021**, *115*, 104050. [CrossRef]
2. Zhang, Z.Q.; Zhao, Y.; Zhang, H.; Zhong, H. Experimental and numerical study on airflow-dust migration behavior in an underground cavern group construction for cleaner production. *Tunn. Undergr. Space Technol.* **2024**, *144*, 105558. [CrossRef]
3. Tao, Y.C.; Hu, H.; Zhang, H.; Zhang, G.; Hao, Z.; Wang, L. A new ventilation system for extra-long railway tunnel construction by using the air cabin relay: A case study on optimization of air cabin parameters length. *J. Build. Eng.* **2021**, *45*, 103480. [CrossRef]
4. Zhang, H.; Sun, J.C.; Zhang, G.; Zhou, X.; Pan, Y. Experimental study on the tunnel temperature distribution under the coupling effect of train blocking and fire inside the carriage. *Tunn. Undergr. Space Technol.* **2021**, *112*, 103915. [CrossRef]
5. Rahimi, S.; Ataee-pour, M.; Madani, H.; Aminossadati, S.M. Investigating the impact of gas emission uncertainty on airflow distribution in an auxiliary ventilation system using CFD and Monte-Carlo simulation. *Build. Environ.* **2021**, *204*, 108165. [CrossRef]
6. Nie, W.; Cai, Y.K.; Wang, L.Y.; Liu, Q.; Jiang, C.W.; Hua, Y.; Cheng, C.X.; Zhang, H.N. Coupled diffusion law of windflow-gas-dust in tunnel energy extraction processes and the location of optimal pollution control exhaust duct. *Energy* **2024**, *304*, 132145. [CrossRef]
7. Liu, N.; Wu, X.; Deng, E.; Ni, E.Q.; Yang, W.C.; Li, G.Z. Dust diffusion laws during partition excavation by boom-type roadheader in a metro tunnel. *Tunn. Undergr. Space Technol.* **2023**, *141*, 105382. [CrossRef]
8. Chen, Z.; Zhao, S.L.; Dong, C.; Wang, S.S.; Guo, Y.B.; Gao, X.; Sun, B.; Chen, W.; Guo, C. Three-stage numerical simulation of tunnel blasting dust diffusion based on field monitoring and CFD. *Tunn. Undergr. Space Technol.* **2024**, *150*, 105830. [CrossRef]
9. Wang, C.Y.; Zhang, H.; Xue, T.; Fang, L. A multi-factor CFD simulation to dust suppression in dynamic tunnel excavation. *Tunn. Undergr. Space Technol.* **2025**, *159*, 106458. [CrossRef]
10. Xu, Y.F.; Wang, S.; Wei, Y.X.; Zhang, Y.R.; Liu, K.H.; Liu, Y.S.; Jin, L.Z. Shengnan Ou Explore the key factors of fine dust particle migration during tunnel construction. *Powder Technol.* **2025**, *452*, 120551. [CrossRef]
11. Liu, J.; Chen, Y.; Wang, W.Q.; Hao, C.W.; Cai, F.; Teng, L.Y.; Luo, X.H. Impact analysis of dust evolution pattern and determination of key ventilation parameters in highland highway construction tunnels. *Heliyon* **2024**, *10*, e33758. [CrossRef] [PubMed]
12. Zhou, B.H.; Qin, B.T.; Zhou, Q.; Gan, J.; Deng, Z.P.; Zhao, F.J.; Ran, M.; Sun, D.W. Hazard and pollution characteristics of rock-containing dust in coal mine tunneling faces based on experimental and numerical study. *Process Saf. Environ. Prot.* **2024**, *192*, 214–229. [CrossRef]
13. Xie, Z.W. Study on Dust Diffusion Law and Numerical Model of Ventilation-Spray Dust Removal in Tunnels Constructed by Drilling and Blasting Method. Bachelor's Thesis, Chongqing University, Chongqing, China, 2023.
14. Liu, H.J.; Wen, X.M.; Lan, J.Q. Study on Equipment Selection, Configuration and Energy-Saving & Environmental Protection Technical Measures for Ventilation, Smoke Elimination and Dust Removal Systems in Extra-Long Tunnels. *Transp. Bus. China* **2022**, *26*, 122–124. [CrossRef]
15. Xue, Y.Q. Study on Ventilation System Layout and Dust Removal Effect of Open-Type TBM Tunnels. *Water Resour. Hydropower Eng.* **2020**, *51*, 98–104.

16. Hu, Y.Z. Study on Dust Removal Efficiency of Negative Ion System During Construction of Long and Large Tunnels. Master's Thesis, Chang'an University, Xi'an, China, 2019.
17. Yin, S.; Nie, W.; Guo, L.; Liu, Q.; Hua, Y.; Cai, X.; Cheng, L.; Yang, B.; Zhou, W. CFD simulations of air curtain dust removal effect by ventilation parametersduring tunneling. *Adv. Powder Technol. Int. J. Soc. Powder Technol. Jpn.* **2020**, *31*, 2456–2468.
18. Nie, W.; Cheng, L.; Yin, S.; Liu, Q.; Hua, Y.; Guo, L.; Cai, X.; Ma, Q.; Guo, C. Effects of press-in airflow rate and the distance between the pressure duct andthe side wall on ventilation dust suppression performance in an excavating tunnel. *Environ. Pollut. Res. Int.* **2022**, *29*, 19404–19419. [CrossRef] [PubMed]
19. Wang, J.; Zhou, G.; Wei, X.; Wang, S. Experimental characterization of multi-nozzle atomization interference fordust reduction between hydraulic supports at a fully mechanized coal mining face. *Environ. Pollut. Res. Int.* **2019**, *26*, 10023–10036. [CrossRef] [PubMed]
20. Sun, Z.Q. Study on Dust Migration Law and Control Technology in Highway Tunnel Construction by Drilling and Blasting Method. Bachelor's Thesis, University of Science and Technology Beijing, Beijing, China, 2015.
21. *ANSYSICEMCFD 17.0*; UserManual, Hexa; ANSYS, Inc.: Canonsburg, PA, USA, 2016; pp. 37–47.

Disclaimer/Publisher's Note: The statements, opinions and data contained in all publications are solely those of the individual author(s) and contributor(s) and not of MDPI and/or the editor(s). MDPI and/or the editor(s) disclaim responsibility for any injury to people or property resulting from any ideas, methods, instructions or products referred to in the content.